# RSC Advances

ROYAL SOCIETY
OF CHEMISTRY

www.rsc.org/advances

# RSC Advances

**Dynamic Article Links** ▶

**PAPER**

# Effect of Pt doping on Gas Sensing properties of porous Chromium Oxide films through Kinetic Response Analysis Approach

**Vinayak B. Kamble[a] and Arun M. Umarji**

The effect of doping trace amount of noble metal (Pt) on the gas sensing properties of chromium oxide thin films, is studied. The sensors are fabricated by depositing chromium oxide films on glass substrate using a modified spray pyrolysis technique and characterized using x-ray diffraction, scanning electron microscopy, transmission electron microscopy and x-ray photoelectron spectroscopy. The films are 10 porous and nanocrystalline with the average crystallite size of ~30 nm. The typical p-type conductivity arises due to presence of Cr vacancies, formed as a result of Cr non-stoichiometry, which is found to vary upon Pt doping. In order to analyze the effect of doping on gas sensing properties, we have adopted the kinetic response analysis approach, which is based on Langmuir Adsorption isotherm (LA) theory. The sensor response is analyzed with equations obtained from LA theory and time constants and energies of 15 adsorption-desorption are evaluated thereof. It is seen that the Pt doping lowers the Schottky barrier height of the metal oxide semiconductor sensor from 222 meV to 172 meV. Subsequently the reduction in adsorption and desorption energies led to the enhancement in sensor response and the improvement in the kinetics of sensor response i.e. response time as well as recovery times of the sensor.

## Introduction

20 Chemoresistive Metal Oxide (MO) semiconductors are one of the most efficient, economic and most commonly used type of gas sensors[1-4]. It shows fairly high and quicker response to a large number of pollutant, toxic and hazardous gases. So far, MOs like ZnO and $SnO_2$ are the most explored gas sensing materials which 25 show good sensitivity and are intrinsically n-type semiconductors[4-7]. However, the lack of selectivity and pronounced humidity effects are the limiting factors[4, 8] for n-type metal oxides and hence has led to increased interest in p-type oxide materials, which show promising gas sensing properties[7, 9-30 11].

The p-type oxides like NiO, $Cr_2O_3$ and $Co_3O_4$ are the potential alternative materials to existing dominating n–type MO semiconductors[9, 10, 12, 13]. Fundamentally the p-type MOs sensors are different from those n-type, as the surface oxygen adsorption 35 causes formation of a surface depletion layer, which is conducting as compared to the resistive core and vice versa in n-type MO[9]. Most of the p-type MO semiconductors are good catalysts and exhibit selective oxidation of particular VOCs and hence, can show essential characteristic of selectivity towards 40 certain VOCs, compared to other gases[9, 10, 14]. However, the major limitation of p-type MOs is the lesser response as compared to its n-type counterparts[15].

The response of MO gas sensors can be successfully improved by functionalization with noble metal catalysts[13, 16]. The noble metal 45 doping is also known to enhance the response kinetics and the catalytic properties of MO[17, 18]. Thus, it leads to reduction in the response time as well as the recovery time and may also induce the selectivity towards a particular gas. Although this dopant induced improvement in sensor properties is knows since a few 50 decades, its origin is still unclear[17, 19]. Hence, in this paper we have studied the gas sensing properties of undoped and Pt doped chromium oxide thin films deposited by Ultrasonic Nebulized Spray Pyrolysis of Aqueous Combustion Mixture (UNSPACM)[11]. The structural, morphological and compositional 55 studies are carried out with gas sensing to study the effect of doping. Further, the Lagmuir based kinetic response analysis approach[20, 21] is adopted to understand the effect of noble metal doping on gas sensing properties of p-type $Cr_2O_3$ films, in order to gain further insight into the mechanism of gas sensing and 60 dopant effect.

## Experimental

### Thin Film deposition

Undoped (CH) and 1 at% Pt doped (CHPt) chromium oxide films 65 were deposited using the novel method of UNSPACM. The details of deposition set up and procedure are described elsewhere[11]. Chromium nitrate nonahydrate ($Cr(NO_3)_3.9H_2O$) and urea were used as starting materials for synthesis. Hexachloroplatinic acid ($H_2PtCl_6$) was used as a source of Pt in 70 the precursor solution and the chemical reaction for 1 at% Pt doping can be written as shown in Eq. (1).
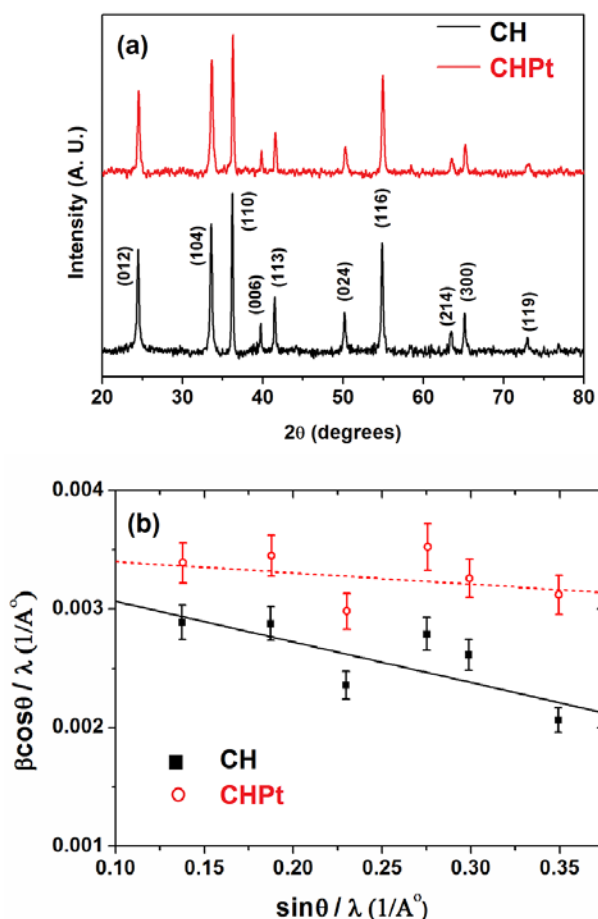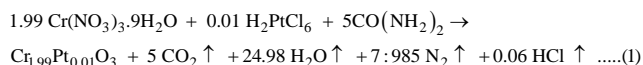
Fig. 1. (a) XRD patterns and (b) Williamson Hall plot of CH ad CHPt films.

$$1.99 \, Cr(NO_3)_3.9H_2O \; + \; 0.01 \, H_2PtCl_6 \; + \; 5CO(NH_2)_2 \rightarrow$$
$$Cr_{1.99}Pt_{0.01}O_3 \; + \; 5 \, CO_2 \uparrow \; + 24.98 \, H_2O \uparrow \; + 7:985 \, N_2 \uparrow \; + 0.06 \, HCl \uparrow \quad .....(1)$$

5 Thus, 1.99 moles of chromium nitrate, 0.01 moles of hexachloroplatinic acid and 5 moles of urea were dissolved aqueous medium to make 0.5 M solution, which was used in the thin film deposition process as precursor solution. The deposition procedure and parameters are discussed elsewhere[11].

10 **Thin film characterizations and gas sensing studies**

The structural studies are done on Panalytical X-pert Pro X-ray diffractometer equipped with accelerated detector and an x-ray source Cu $K_\alpha$ wavelength (1.5418 A$^o$), in step size $0.02^o$ /sec. The scanning electron microscopy (SEM) studies of the films are 15 carried out on FEI insitron FESEM. Besides, the crystallinity, size, and the morphology were investigated using a Transmission Electron Microscope (TEM) (Model JEOL 2100F, 200 keV). The X-ray photoelectron spectrums (XPS) were recorded on an Axis Ultra DLD (From Kratos) high resolution instrument with auto 20 charge neutralization having Mg $K_\alpha$ source radiation (1253.5 eV). The binding energies were also confirmed by comparison with graphite at 284.5 eV having an accuracy of ±0.3 eV. The gas sensing studies are carried out on in-house built gas sensor characterizations system, the details can be found in our previous 25 paper[11]. The response (S) is calculated as S=ΔR/R, where R is the

sensor resistance in air and ΔR is the change in resistance upon exposure to test gas.

## Results

### X-ray Diffraction (XRD)

30 The XRD patterns of both the CH and CHPt films are shown in Fig. 1(a). Both the patterns agree well with JCPDS data of pure $Cr_2O_3$ phase and do not show any impurity peak within the limit of detection. However, the XRD peaks of CHPt show slightly higher broadening, which implies smaller crystallite size in case 35 of CHPt. The crystallite sizes are calculated using Scherrer formula and are found to be nearly 30 and 25 nm for CH and CHPt films respectively. The doping is not found to affect the crystallinity, but the XRD peak exhibits a shift towards higher 2θ, (see Fig. S1 in Supplimentary information section), which implies 40 an increase in the d-spacing.

The XRD data was further analyzed with Williamson-Hall (W-H) relation[22] (see Eq. (2))

$$\frac{\beta \cos \theta}{\lambda} = \frac{1}{D} + \varepsilon \frac{\sin \theta}{\lambda} \qquad ...(2)$$

45 The W-H plot (i.e. βcosθ/λ vs. sinθ/λ) for CH and CHPt films is shown in Fig. 1(b). The slope of the straight line represents the effective strain (ε) in the lattice. The ε values of CH and CHPt are estimated as -0.342 and -0.0094 respectively. The negative sign represents a compressive strain in the lattice[23, 24]. The reduction in 50 magnitude of ε in CHPt implies reduction in the compressive strain in the lattice. It could be, as a result of Pt incorporation in the lattice, due to comparable size of ionic radii of $Cr^{+3}$ and $Pt^{+4}$ (i.e. 75.5 and 76.5 pm respectively).
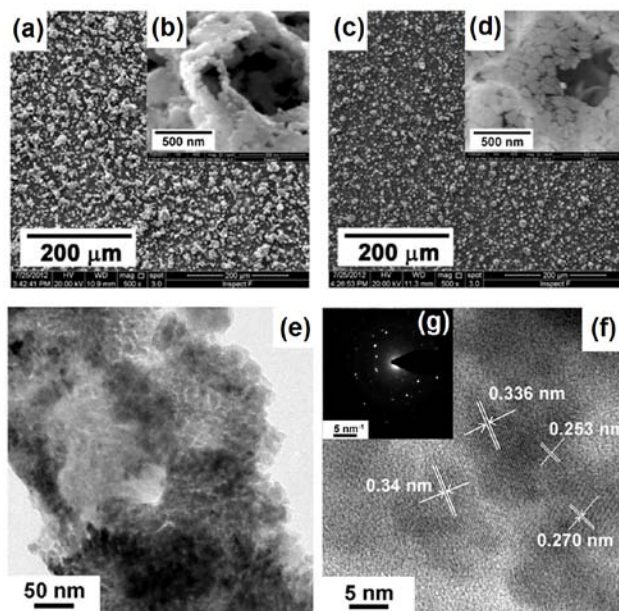
55 **Electron Microscopy**



Fig. 2. The SEM micrographs of (a) and (b) CH film and (c) and (d) of CHPt films. (e) TEM image, (f) HRTEM image and (g) SAED patern of CHPt film.
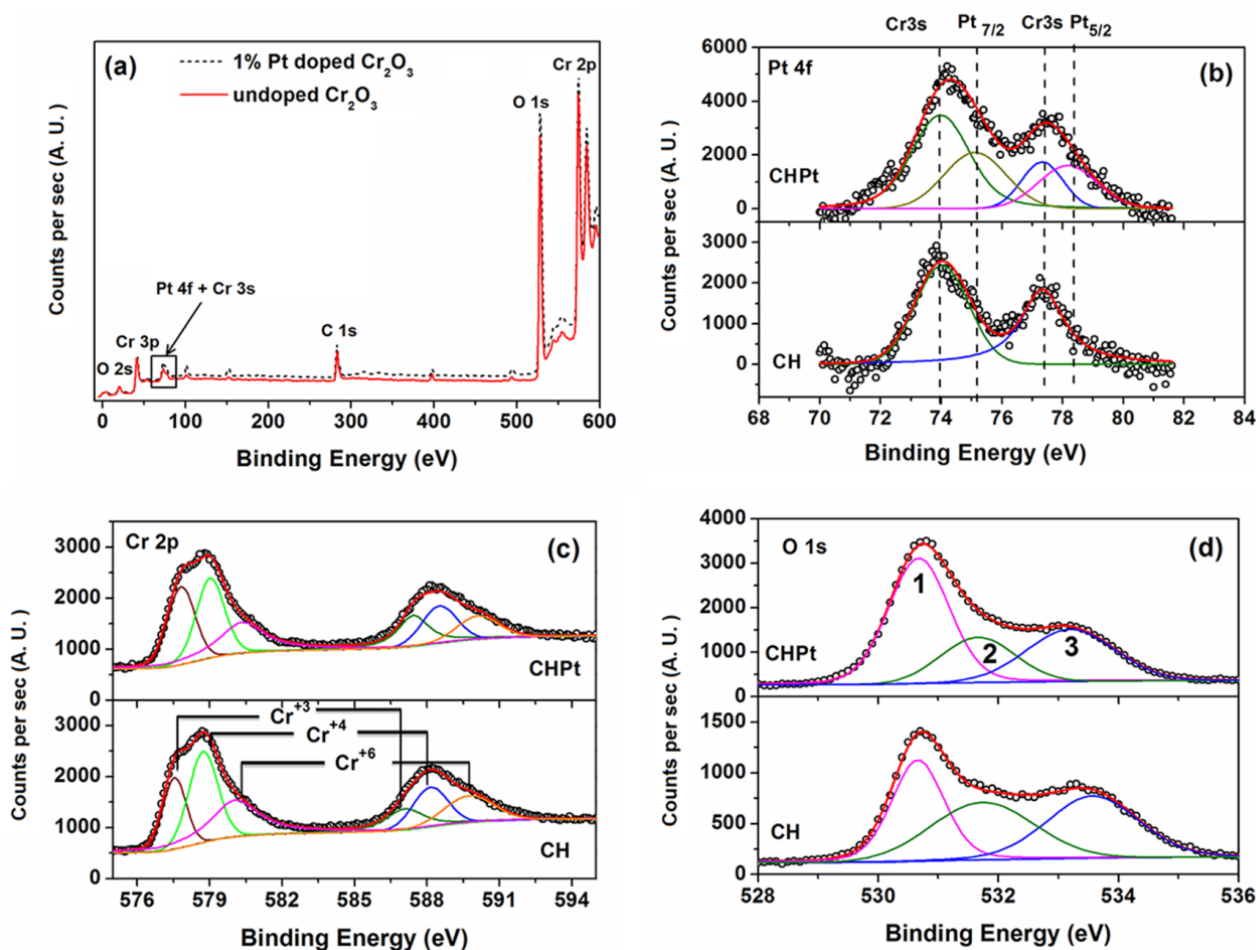
Fig. 3. Comparison of (a) survey XPS spectrum and (b) Pt4f, (c) Cr2p and (d) O1s regions of XPS spectra of Ch and CHPt films.

The Electron Microscopy images of CH and CHPt films are depicted in Fig. 2. It is seen from SEM results, that the films are composed of few micron sized spheres on film surface, which are further composed of nanosized particles (crystallites) which are typically ~50 nm in size. Fig. 2(a) shows the SEM image of CH film showing uniform large area deposition (typically $500 \times 500$ $\mu m^2$ area) while, the inset shows enlarged view of the films at higher magnification with visible particle size and average pore size of ~500 nm. Although CHPt films does not show significant change in the film morphology (see Fig. 2(c)) and the porosity (See Fig. 2 (d)), the similar particle size is fairly evident from the magnified image shown in Fig. 2(d). This agrees well with findings of XRD results. A set of cascading SEM images can be found in Supplementary information section (see Fig. S2). Thus, from SEM results the average pore size and the particle size (i.e. crystallite size from XRD) are nearly the same in both, the doped and undoped films. Hence, it may be assumed that the surface area of both the films does not differ significantly.

The Transmission Electron Microscopy (TEM) images of the material scraped from CHPt films (shown in Fig 2(e)), confirms the nanocrystalline nature of the as-deposited films. However, the inter-particle adhesion of the film is so strong that 3 hrs of sonication of the scraped sample does not suffice to separate the individual crystallites. The High resolution TEM (HRTEM) (Fig. 2(f)) images reveal the different planar spacings of 0.336, 0.340 and 0.270 nm corresponding to (hkl) reflections of (012), (012) and (104) respectively, Further, the Selected Area Electron Diffraction (SAED) pattern in the inset in Fig. 2(g), also depicts the crystallinity of the as-prepared films.

### X-ray Photoelectron Spectroscopy (XPS)

The chemical stoichiometry of oxide film surface is examined with XPS and the spectra of CH and CHPt films are shown in Fig. 3. Fig. 3(a), shows the comparison of survey XPS spectra of CH and CHPt films. Further, the Pt 4f region of XPS spectra is analyzed and presented in Fig. 3(b). Here, the Pt 4f peaks are found to overlap with the Cr 3s peak and hence the spectrum is deconvoluted to examine the oxidation state of Pt. The region consists of four peaks, two of which are due to multiplet splitting of Pt 4f J=7/2 and 5/2 while the other peaks belonging to Cr 3s with its satellite. In a paramagnetic atom like Cr, the ejection of core s electron leads to two lines, as the energies of up an down spin electrons differ significantly, due to the difference in the effect of exchange interaction. Hence the Cr 3s satellite appears due to unpaired Cr 3s electron to account for stability of the Cr 3d
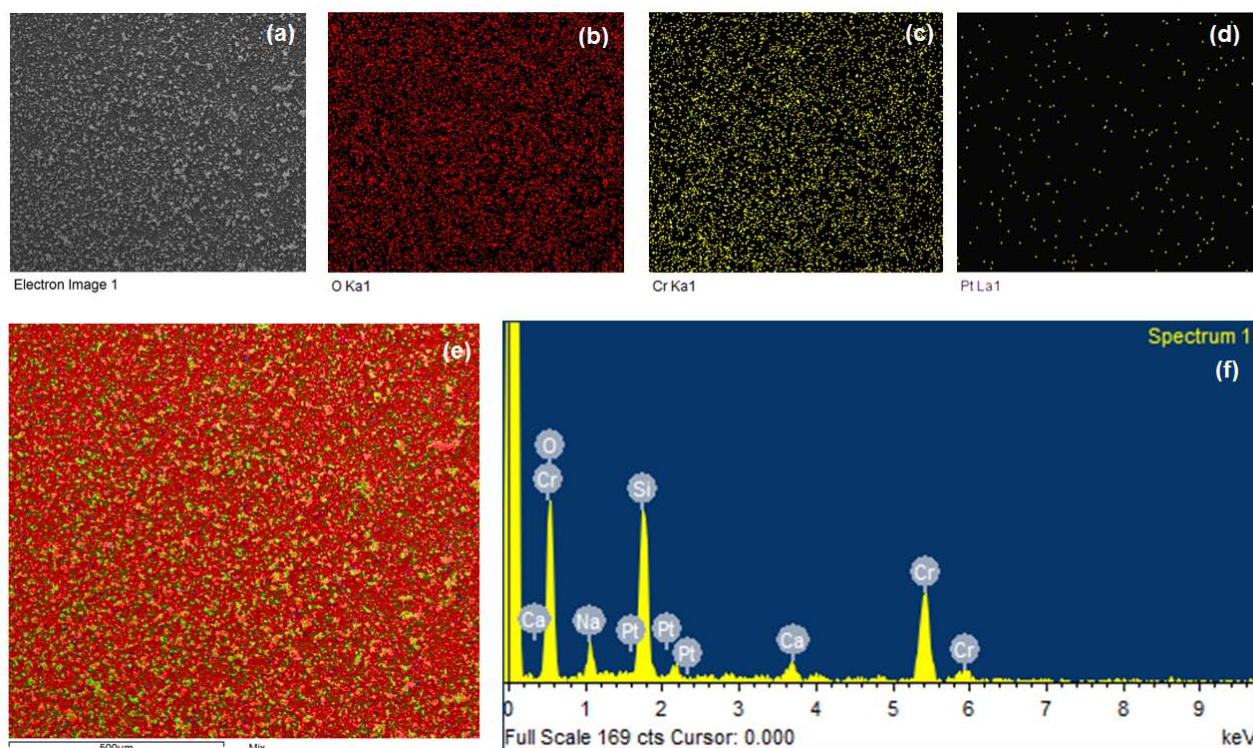
Figure 4. The EDS mapping results of CHPt film showing (a) electron image, (b) Oxygen, (c) Chromium, (d) Platinum elemental maps, (e) the mixed map and (f) the EDS spectrum of the film.

shell by making it exactly half filled ($d^5$).

TABLE1. Summery of relative ratio of O1s line Cr oxidation states and Cr:Pt ratio calculated from XPS deconvolution data.

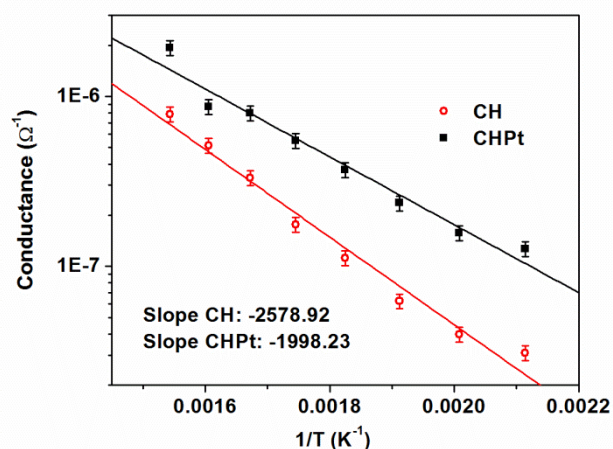|  | CH | CHPt |
|---|---|---|
| Cr2p (1(+3) : 2(+4) : 3(+6)) | 31 : 35 : 34 | 48 : 30 : 22 |
| O1s (1 : 2 : 3) | 31 : 46 : 23 | 39 : 42.5 : 18.5 |
| Pt 4f (Cr:Pt ratio) | - | 99.2 : 0.8 |



Fig. 5. The Arrhenius plots of as-prepared CH and CHPt films in the temperature range 200 - 400 °C.

Fig. 3(c), shows the comparison of deconvoluted Cr 2p region of XPS spectrum. Both the films show the mixed valance nature of Cr; however the relative percentage of Cr varies significantly and is summarized in Table. I. The quantification is done using XPS cross sectional data provided in reference no. 22[25] Further, similar degree of variation is also seen in O 1s spectrum (see Fig. 3(d)). The line 1 in O 1s spectrum corresponds to lattice oxygen ($O^{-2}$), which shows a significant increase upon Pt incorporation (by ~10%) (see Table. I) along with increase in $Cr^{+3}$ (by ~17%). Here, the oxidized state of Pt (i.e. $Pt^{+4}$) implies that the in-situ oxidation of Pt has taken place during the deposition, which leads to the enhanced reduced state of Cr (i.e. $Cr^{+3}$). Further, as the kinetic energy of the ejected photoelectron is majorly affected by the local chemical environment of the parent atom/ion, the smaller binding energy variations could also be due to the incorporation of $Pt^{+4}$ ion in the crystal. The line 2 in Fig. 3(d), is attributed to non-stoichiometry in Cr valance in CHPt. Here, line 2 has reduced compared to CH, which also signifies reduced non-stoichiometry due to enhanced $Cr^{+3}$. Further similar reduction is also seen in line 3 of O 1s which is ascribed to surface adsorbed –OH and –$O_2$ groups.

**Energy Dispersive Spectroscopy (EDS) Mapping**

To further confirm the presence of Pt and to study the dopant distribution the EDS mapping of the films was done. Fig. 4 shows the results of EDS analysis i.e. the individual elemental maps (Fig. 4a-d) along with the overlapped mix map (Fig. 4e) and the EDS spectrum (Fig. 4f). As seen from Fig. 4, the films exhibit very uniform Pt dopant distribution and also the quantification yields 0.6% Pt and 99.4% Cr. Although the resolution limit of EDS spectroscopy is 5%, these results are fairly in accordance with that of nominal composition and support the XPS quantification results. The presence of Si, Na and Ca in EDS

spectrum is identified from the soda-lime glass substrate of the films.

### Schottky barrier height estimation using Arrhenius equation

5 The evaluation of the effect of Pt doping on the activation energy of the sensor is done with the help of the Arrhenius equation as shown in Eq. (3)[26, 27] in the temperature range $200 - 400 \ ^oC$.

$$G = G_0 \exp[-\Phi / kT] \qquad (3)$$
$$\text{i.e. } \log G = -(\Phi / k) \times (1 / T) + \log G_0 \qquad (3a)$$

Where, G and $G_0$ are instantaneous and initial conductance, $\Phi$ is the Schottky barrier height for change in conductance of the 10 materials at absolute temperature T (K). The sensor is equilibrated at different temperatures in the range $200 - 400 \ ^oC$ at regular intervals of 25 $^oC$ and the sensor resistance is measured. The log of inverse of resistance (i.e. conductance) is plotted against the reciprocal of the absolute temperature. Both the plots 15 follow linear nature (as seen in Fig. 4) and the activation energy is evaluated from the slopes. The values of $\Phi$ calculated from slopes are 222 and 172 meV for CH and CHPt films respectively. Thus, the Pt doping results in the reduction of thermal Schottky barrier, making it favourable for sensing action energetically.

### 20 Gas sensing studies

The gas sensing studies of both the undoped and doped as-deposited films are undertaken, which demonstrates the characteristic p-type behavior of chromium oxide films. The film resistance decreases upon exposure to oxidizing gas like $NO_2$ and 25 increases for the reducing gas like ethanol vapors (See Fig. S3 in supporting information). Fig. 5 shows, the effect of doping on the gas sensor response at different temperatures for different gases, namely $NO_2$, $CH_4$ and ethanol (EtOH) for both CH and CHPt films. Although the doping is found to result in enhancing the 30 response towards all the gases studied, the maximum response temperature is found to be lowered for $NO_2$, increased for $CH_4$ and does not show significant change in case of ethanol gas.

### Kinetic analysis of gas sensing response to ethanol vapors

35 The chromium oxide films show relatively high response to

ethanol gas as compared to other gases studied and the Pt doping is found to enhance the sensitivity and improve response as well as recovery times. Hence, the kinetics of sensor response has been studied by Langmuir isotherm model to analyze the effect of 40 Pt doping[20, 21, 28, 29].
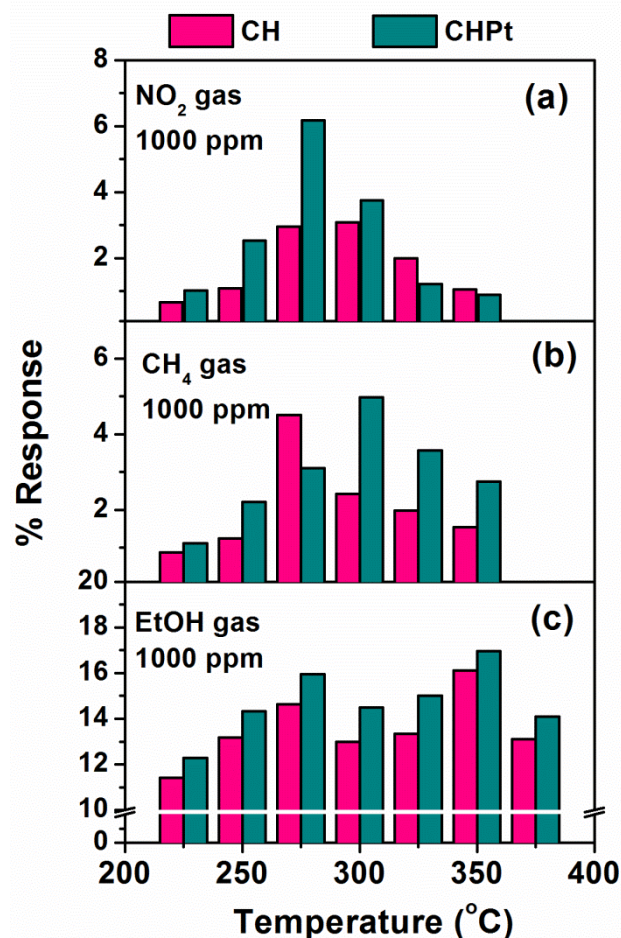


Fig. 6. The variation of response with temperature for 1000 ppm (a) $NO_2$, (b) $CH_4$ gases and (c) ethanol vapors for CH and CHPt films.
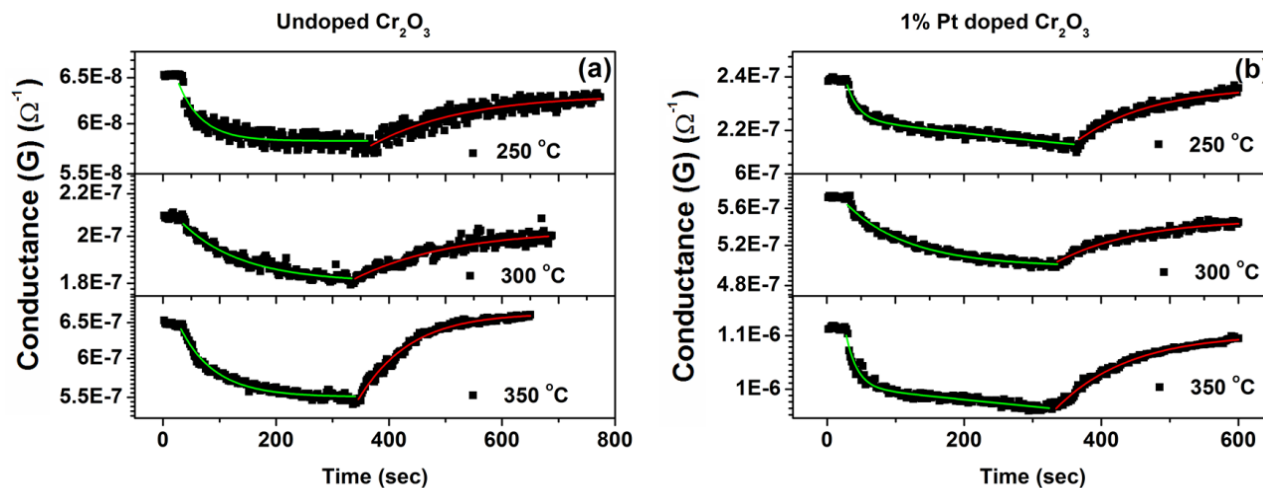


Fig. 7. The fitting of response transients (a) CH and (b) CHPt films towards 1000 ppm of ethanol vapors at various temperatures.
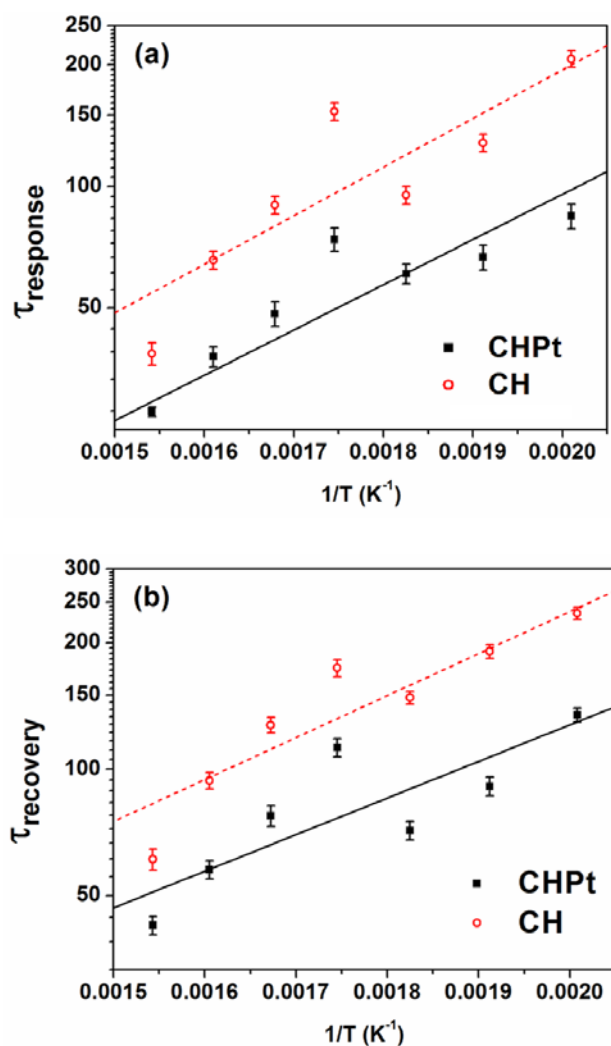
Fig. 8. The variation of (a) response and (b) recovery time constants with reciprocal of absolute temperature.

Where, $G(t)$ and $G'(t)$ are instantaneous conductance for response and recovery kinetics. These time constants also follow Arrhenius type of the exponential dependence (see Eq. (6) and (7)) with the
25 inverse of the temperature with the corresponding energies giving adsorption and desorption energies for response and recovery times respectively[20, 30, 31].

$$\tau_{response} = \tau_o \exp(-E_a/kT) \qquad (6)$$

$$\tau_{recovery} = \tau_o \exp(-E_d/kT) \qquad (7)$$

Where, $E_a$ and $E_d$ are adsorption and desorption energies
30 respectively, and k is Boltzmann constant ($8.617 \times 10^{-5}$ eV/K) and T is absolute temperature. Hence, the $\tau$ values obtained from the fitting data are plotted against the reciprocal of absolute temperature and the values of adsorption ($E_a$) and desorption ($E_d$) energies are calculated from the slope of the plots shown in Fig. 8
35 and the values are summarized in Table 2. It is evident from the values of $E_a$ and $E_d$ that Pt incorporation leads to decrease in the adsorption / desorption energies which govern the response time and recovery times of the sensor respectively.
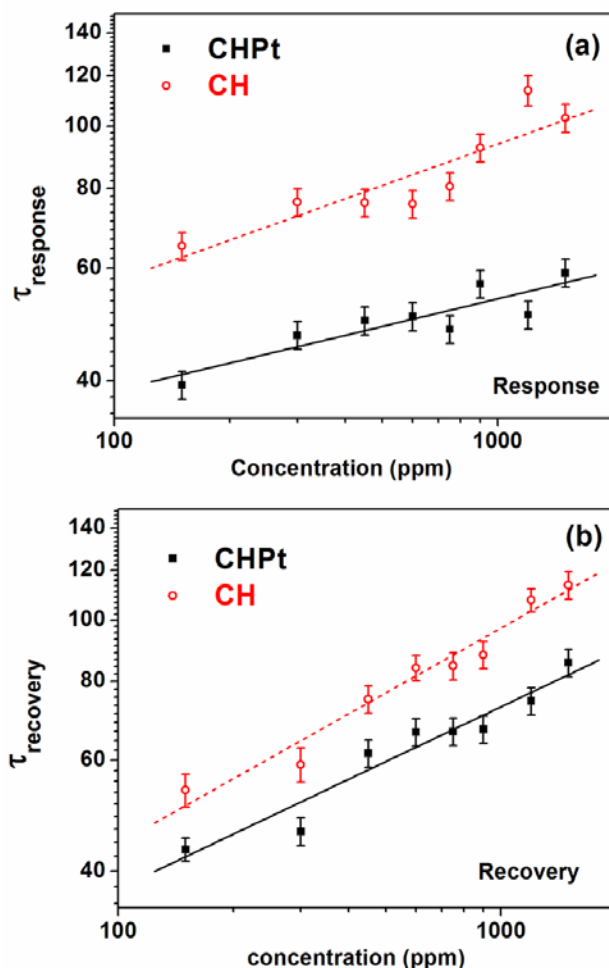


40 Fig. 9. The variation of (a) response and (b) recovery time constants with ethanol concentration

5
**Variation of response time with temperature**

The response transients of the CH and CHPt film sensor for ethanol gas are carefully analyzed at all the temperatures. It is seen that the Pt incorporation indeed led to faster response time
10 and recovery time (see Fig. S4, in supplementary information). As the temperature increases, the sensor shows quicker response and speedy recovery. The typical time constant values are obtained by fitting the response transients with relations obtained from the Langmuir - isotherm model[20, 21, 28, 29] (i.e. Eq. (4) and
15 Eq. (5)) and the characteristic time constants ($\tau$) are evaluated. The satisfactory fittings are obtained considering only one active site for adsorption (i.e., only one exponential term considering one active site of adsorption) and the fittings are shown in Fig. 5.

$$G(t)_{response} = G_0 + G_1[\exp(-t/\tau_{response})] \qquad (4)$$

20 and,

$$G'(t)_{recovery} = G'_0 + G'_1[1 - \exp(-t/\tau_{recovery})] \qquad (5)$$

However, the larger standard deviation of the actual experimental data in Fig. 8.; accounts for the complex nature of the process and

its dependency on several factors such as surface area, stoichiometry and the crystallite size, but the values obtained give a close estimate.

5 TABLE 2.The adsorption and desorption energies calculated by fitting experimental data.

| Sample | Response | | Recovery | |
|---|---|---|---|---|
| | Slope ($E_a$/k) | $E_a$ (meV) | Slope ($E_d$/k) | $E_d$ (meV) |
| CH | 1204.52 | 103.8 ± 26.7 | 766.38 | 66.03 ± 19.7 |
| CHPt | 1121.39 | 96.63 ±14. 93 | 655.07 | 56.45 ± 14.7 |

**Variation of response time with concentration**

The response of CH and CHPt films towards various concentrations of ethanol was further studied using power law of 10 metal oxide semiconductor gas sensors, as shown in Eq. (8).

$$S = AC^\beta \qquad (8)$$
$$\text{i.e.} \log S = \beta \log C + \log A \qquad (8a)$$

Where, S is sensor response, C is concentration of test gas, A is prefactor and β is the exponent, which can have values 0.5 or 1. The log-log plot of response with the respective concentrations as 15 given by Eq. (8a) is plotted (See in Fig. 9). As expected, the data does satisfactorily exhibit a linear fit. The values of β for CH and CHPt are 0.495 and 0.386 respectively. This signifies similar nature of surface reaction for both doped as well as undoped films.
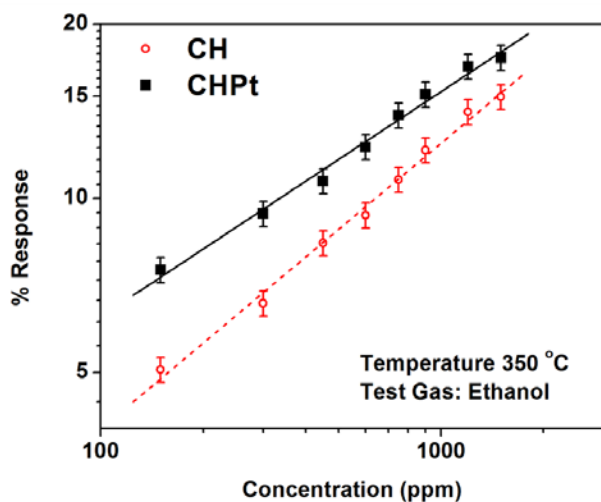


20
Fig. 10. The log-log plot of response Vs. concentration of test gas i.e. ethanol for CH and CHPt films.

## Discussion

The dopants and additives like noble metals (Pt, Pd or Au) or 25 other metal oxides are known to enhance the sensor characteristics. The phenomenon is well explained through mechanisms like spillover or Fermi energy control[1, 4, 19, 32]. However, these models are able to explain the improvements in only qualitative manner. Hence, in order to quantify the measure 30 of improvements due to the introduction of dopants or additives, it is necessary to represent it in terms of parameters like response, the time constants for response as well as recovery and the goodness of fit (GoF) for the model.

35 In light of the above analysis, we can say that the incorporation of

noble metal led to enhancement in the sensory properties like sensitivity and response as well as recovery times. The values of adsorption and desorption energies found from the fitting data implies that Pt incorporation significantly decreases the 40 adsorption and desorption energies (see Table 2). Further, this reduction in adsorption-desorption energy facilitates higher surface coverage (θ) of the test gas molecules on the sensor surface. This is due to the transduction function of the sensor material, which leads to enhancement in the change of charge 45 carrier density, which in turn results in a higher change in resistance and is estimated in terms of sensor response (S). As mentioned earlier the results of the model fitting are evaluated in terms of GoF and are summarized in Table 3.

50 In statistics, the GoF is estimated using reduced Chi square ($\chi_{red}^2$). It is a measure of the degree of variation between expected and actual data. $\chi_{red}^2 >> 1$ means a poor fitting, while $\chi_{red}^2 \sim 1$ or slightly lesser than 1 indicates that the extent of the match between observations and estimated value is in accord with the 55 error variance. However $\chi_{red}^2 << 1$ indicates over-fitting and the error variance has been over-estimated. As seen from, Table 3, the values of $R^2$ are almost approaching 1 (except nearly 0.8 for τ, which is also considerably fair, due to its complex nature) and that of $\chi_{red}^2$ also in fair accordance with the expected satisfactory 60 fit. Thus the Langmuir model for kinetic response analysis satisfactory establishes quantification for the improvement of sensing parameters after Pt incorporation in chromium oxide film.

Table 3. The quantitative summary of the goodness of fit (GoF) of the 65 model in terms of $R^2$ and reduced $\chi_{red}^2$.

| | CH | | CHPt | |
|---|---|---|---|---|
| | $R^2$ | $\chi_{red}^2$ | $R^2$ | $\chi_{red}^2$ |
| G= $G_0 \exp(-\Phi/kT)$ | 0.975 | 0.039 | 0.962 | 0.036 |
| G= $G_0 + G1 \exp(-t/\tau)$ | >0.90 | <0.5 | >0.90 | <0.5 |
| $\tau = \tau_0 \exp(-Ea/kT)$ [response] | 0.801 | 0.52 | 0.872 | 1.49 |
| $\tau = \tau_0 \exp(-Ed/kT)$ [recovery] | 0.845 | 0.73 | 0.791 | 1.07 |
| S=$AC^\beta$ | 0.993 | 0.019 | 0.988 | 0.012 |

## Conclusion

In conclusion, the novel solution based technique of UNSPACM has successfully led to the incorporation of 1 at% Pt dopant into the chromium oxide thin films and the actual stoichiometry 70 calculated from XPS reveals nearly same concentration of Pt dopant into the lattice. This trace amount of noble metal doped in chromium oxide films is seen to improve its gas sensing characteristics, i.e. both in terms of response and response time /recovery time. The gas sensing response studied by using the 75 Langmuir-isotherm model with kinetic response analysis reveals that the incorporation of 1 at% Pt dopant improves the kinetics of surface processes such as adsorption and desorption by lowering the corresponding energies. This reduction in adsorption-desorption energy facilitates enhanced surface coverage of the 80 test gas molecules, which further results into the enhancement in the change in sensor resistance. Further, from GoF data, it can be seen that the Langmuir − isotherm model satisfactorily explains that the reduction in energetic parameters play a decisive role in enhancing the sensor kinetics.

## Acknowledgements

## Notes and references

*a Materials Research Centre, Indian Institute of Science, Bangalore, India 560012; E-mail: vinbk@mrc.iisc.ernet.in*
† Electronic Supplementary Information (ESI) available: [details of any supplementary information available should be included here]. See DOI: 10.1039/b000000x/

1. C. O. Park and S. A. Akbar, J. Mater. Sci., 2003, 38, 4611-4637.
2. N. Yamazoe, Sens. Actuators, B, 2005, 108, 2-14.
3. M. Tiemann, Chemistry – A European Journal, 2007, 13, 8376-8388.
4. C. Wang, L. Yin, L. Zhang, D. Xiang and R. Gao, Sensors, 2010, 10, 2088-2106.
5. V. B. Kamble and A. M. Umarji, Appl. Phys. Lett., 2014, 104, -.
6. W. Gopel and K. D. Schierbaum, Sens. Actuators, B, 1995, 26, 1-12.
7. G. Korotcenkov, Mater. Sci. Eng., B, 2007, 139, 1-23.
8. R. G. Pavelko, A. A. Vasiliev, E. Llobet, V. G. Sevastyanov and N. T. Kuznetsov, Sens. Actuators, B, 2012, 170, 51-59.
9. H-J Kim and J-H Lee, Sens. Actuators, B, 2014, 192, 607 - 627.
10. L. Wang, J. Deng, Z. Lou and T. Zhang, Sens. Actuators, B, 2014, 201, 1-6.
11. V. B. Kamble and A. M. Umarji, J. Mater. Chem. C, 2013, 1, 8167-8176.
12. G. Zhu, C. Xi, H. Xu, D. Zheng, Y. Liu, X. Xu and X. Shen, RSC Adv., 2012, 2, 4236-4241.
13. A. Kasikov, A. Gerst, A. Kikas, L. Matisen, A. Saar, A. Tarre and A. Rosental, Cent. Eur. J. Phys., 2009, 7, 356-362.
14. A. S. Zoolfakar, M. Z. Ahmad, R. A. Rani, J. Z. Ou, S. Balendhran, S. Zhuiykov, K. Latham, W. Wlodarski and K. Kalantar-zadeh, Sensors and Actuators B: Chemical, 2013, 185, 620-627.
15. N. Barsan and U. Weimar, J. Electroceram., 2001, 7, 143-167.
16. M. V. Vaishampayan, R. G. Deshmukh and I. S. Mulla, Sens. Actuators, B, 2008, 131, 665-672.
17. M. Schweizer-Berberich, J. G. Zheng, U. Weimar, W. Gopel, N. Barsan, E. Pentia and A. Tomescu, Sens. Actuators, B, 1996, 31, 71-75.
18. N. Yamazoe, Sens. Actuators, B, 1991, 5, 7-19.
19. N. Yamazoe, Y. Kurokawa and T. Seiyama, Sens. Actuators, B, 1983, 4, 283 - 289.
20. K. Mukherjee and S. B. Majumder, J. Appl. Phys., 2009, 106, 064912-064910.
21. K. Mukherjee, D. C. Bharti and S. B. Majumder, Sens. Actuators, B, 2010, 146, 91-97.
22. V. D. Mote, Y. Purushotham and B. N. Dole, J Theor Appl Phys, 2012, 6, 1-8.
23. N. Mazumder, A. Bharati, S. Saha, D. Sen and K. K. Chattopadhyay, Curr. Appl Phys., 2012, 12, 975-982.
24. A. K. Zak, W. H. Abd. Majid, M. E. Abrishami and R. Yousefi, Solid State Sci., 2011, 13, 251-256.
25. J. J. Yeh and I. Lindau, At. Data Nucl. Data Tables 1985, 32, 1-155.
26. C. O. Park and S. Akbar, Journal of materials science, 2003, 38, 4611-4637.
27. I-D Kim, A. Rothschild, T. Hyodo and H. L. Tuller, Nano Lett., 2006, 6, 193-198.
28. S. Strassler and A. Reis, Sens. Actuators, B, 1983, 4, 465-472.
29. S. Aygun and D. Cann, J. Phys. Chem. B, 2005, 109, 7878-7882.
30. G. Korotcenkov, V. Brinzari, V. Golovanov and Y. Blinov, Sens. Actuators, B, 2004, 98, 41-45.
31. V. Brynzari, G. Korotchenkov and S. Dmitriev, Sens. Actuators, B, 1999, 61, 143-153.
32. S. R. Morrison, Sens. Actuators, B, 1987, 12, 425-440.

**RSC Advances Accepted Manuscript**
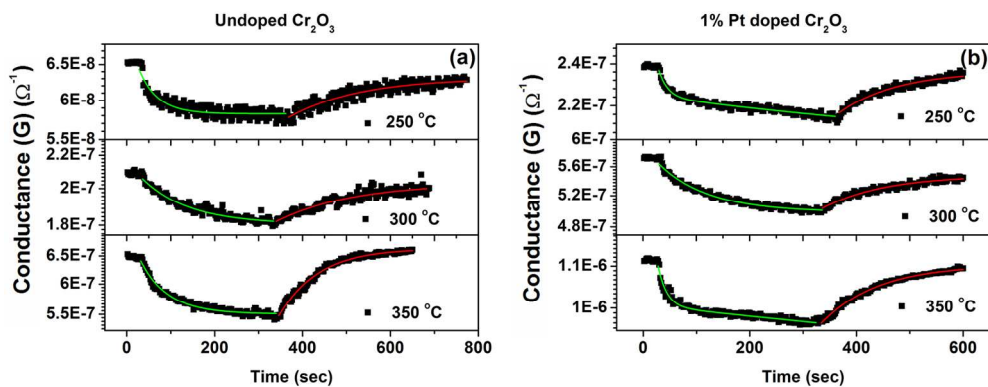
The fitting of response transients (a) undoped (CH) and (b) 1% Pt doped (CHPt) Cr2O3 films for 1000 ppm of ethanol vapors at various temperatures.